Three-Dimensional Curvy Electronics Enabled by Conformal Additive Stamp Printing

Kyoseung Sim[1], Song Chen[1], Zhengwei Li[2], Zhoulyu Rao[3], Jingshen Liu[4], Yuntao Lu[3], Seonmin Jang[3], Faheem Ershad[5], Ji Chen[4], Jianliang Xiao[2], and Cunjiang Yu[1,3,4,5,6]*

[1]Department of Mechanical Engineering, University of Houston, Houston, TX 77204 USA

[2]Department of Mechanical Engineering, University of Colorado, Boulder, CO 80309, USA

[3]Materials Science and Engineering Program, University of Houston, Houston, TX 77204 USA

[4]Department of Electrical and Computer Engineering, University of Houston, Houston, TX 77204 USA

[5]Department of Biomedical Engineering, University of Houston, Houston, TX 77204, USA

[6]Texas Center for Superconductivity, University of Houston, Houston, TX 77204, USA

*Correspondence to: cyu15@uh.edu

Keywords: balloon, transfer printing, curvilinear surface, conformal printing, 3D electronics

Abstract

The dominant form of electronics, i.e. microelectronics, have been traditionally manufactured into planar layouts. Many electronics and devices, ranging from optoelectronics to wave electronics and to wearables, need to be configured into three dimensional (3D) curvy shapes to realize their functions. However, so far, there has been very limited success in realizing them, mainly due to the lack of effective manufacturing technology. Here, we reported conformal additive stamp (CAS) printing technology for reliably manufacturing 3D curvy electronics in a simple and effective way. CAS printing employs a pneumatically inflated elastomeric balloon as a conformal stamping medium to pick up the pre-fabricated electronic devices and print them onto curvy surfaces. Various devices in curvy shapes, including Si pellets, photodetector arrays, electrically small antennas, hemispherical solar cells, and smart contact lenses are demonstrated based on CAS printing. CAS printing is versatile as it can manufacture onto arbitrary 3D surfaces. Systematic investigations have revealed the key aspects, fidelity, and versatility of CAS printing. CAS printing opens doors towards the burgeoning 3D curvy electronics.

Introduction

The dominant form of electronics, i.e. microelectronics, have been traditionally manufactured into planar layouts. However, there are many devices required to pursue 3D shapes, whose performances and functionalities are strongly coupled with their geometrical form factors. Examples include imagers with curved focal planes[1-4], electronics enabled smart contact lenses with curvilinear shapes[5-7], and antennas with non-planar designs[8-10] among others. These types of devices in 3D curvilinear layouts, especially in the size range from millimeters to centimeters with feature sizes and accuracy on the order of microns, are technically very challenging to build. The major hurdle lies in the lack of a proper versatile manufacturing technology to construct 3D curvy electronics. A reliable and versatile manufacturing approach has not been reported before.

Existing electronics manufacturing technologies, such as microfabrication, cannot achieve 3D curvilinear electronics due to the incompatible inherent two-dimensional (2D) nature of the established wafer based planar processes. On the other hand, some emerging manufacturing technologies could possibly provide venues to address the manufacturing challenge directly or indirectly, but they all have major deficiencies. For instance, deterministic folding processes have been used to deform a predefined 2D sheet into 3D shapes[11-14]; yet, it has limited access to non-developable shapes, such as spherical or arbitrary complex curvilinear shapes. 3D printing has been exploited to manufacture electronics by delivering electronic inks directly onto curved surfaces[8,15-17]; however, 3D printing is mainly applicable for slurry based inks, thus the fabricated devices cannot achieve comparable high performances compared with those from wafer based technologies, due to the inherent material limitations. Another approach involves pre-stretching and flattening a curvy elastomeric membrane as a temporary flat substrate for planar device fabrication and then releasing to form curved shapes[18-20]. However, rubber is one of the very few materials that can be stretched from curvy to flat shapes, even if the large mechanical strain associated with the flattening and restoring steps is disregarded; therefore, the approach restricts its general usage and visibility.

Here, we report a novel manufacturing technology, namely conformal additive stamp (CAS) printing, to reliably manufacture devices with 3D shapes in an easy and adaptable manner. In this study, CAS printing employs a pneumatically inflated elastomeric balloon as a conformal stamping medium to pick up the pre-fabricated electronic devices (i.e. inks) in 2D geometries from pervasive microfabrication and then deliver them onto random curvilinear 3D surfaces. The process, schematically illustrated in Fig. 1a, involves firstly approaching a pneumatically inflated balloon stamp to the fabricated inks. The stamp is then brought into intimate contact with the fabricated inks. Due to the excellent deformability, the balloon stamp is able to conformably contact and pick up the inks when peeled off. The inked balloon stamp is then brought into contact with the target 3D curvilinear surfaces to directly deliver or print the inks on. The excellent deformability of the elastomeric balloon allows it to form intimate contact with complex 3D surfaces and thus, it can print inks on 3D substrates. A distinct feature of CAS printing is that it allows 1) the construction of high-performance electronics by taking the advantage of microfabrication and 2) the manufacture on random 3D curvy shapes, which outperforms any possible approaches to the best of our knowledge. Systematic experimental, computational, and analytical studies of the CAS printing technology and several demonstrated example devices ranging from isolated pixel arrays to interconnected functional devices reveal the key aspects, fidelity, and versatility of CAS printing.

Results

CAS printing of Si pellet array

Figure 1a shows the schematic illustration of a CAS printed Si pellet array. The process involves preparing a Si pellet array on a temporary substrate, picking up the array using a balloon stamp, and printing the array onto a 3D curvy surface. The Si pellet array (39 × 39, each pellet size: 100 µm × 100 µm) was fabricated based on a silicon-on-insulator (SOI) wafer with 1.25 µm-thick top Si. The processes mainly include photolithography and active-ion etching (RIE) to define the pellet geometries, formation of photoresist anchors as temporary tethers, and undercut etching of the buried oxide in concentrated hydrofluoric acid (HF, 49%) to separate the pellets from the substrate. The detailed processes are described in the Methods and Supplementary Fig. 1. The photograph image (left) and optical microscopy image (right) of the prepared Si pellet array on a wafer are shown in Supplementary Fig. 2. The balloon stamp was prepared by coating a thin layer (~271 µm) of Clearflex (Smooth-On, Clear Flex^{TM} 50) on the surface of a commercially available latex balloon (Qualatex, 5 in. round). Clearflex was chosen because of two major reasons: 1) the ability to coat on the latex balloon surface, and 2) modifiable surface adhesion for picking up and printing.

A custom-made CAS printing platform is shown in Supplementary Fig. 3. The balloon stamp is able to move up and down. The prepared balloon stamp was moved down to press against the wafer to contact with the array and then the stamp was lifted off to pick up the array from the wafer. The temporary photoresist tethers were broken due to the adhesion between the pellet and Clearflex[21-23]. Figure 1b shows the images of the Si pellet array on the balloon stamp upon picking up. The Si pellet array was finally printed onto a hemispherical shaped Ecoflex (Smooth-On Ecoflex 00-30) shell, which was prepared based on a molding process (Supplementary Fig. 4). It is noted that the outer surface of the hemispherical shell was treated by ultraviolet-ozone (UVO) for 10 min to generate hydroxyl terminal groups which allow for covalent bonding with Si pellets.

Similar surface treatment was employed in other studies[24-26]. Figure 1c shows the image of the Si pellet array on the hemispherical shell. The inset is the optical microscopic image. It is noted that no cracks or damage of the Si pellets was observed during the CAS printing process. In addition, the yield of both picking up and printing were 100%.

The associated deformation and strain in both the balloon stamp and the Si pellet array during and after CAS printing were investigated by finite element analysis (FEA). The details of the FEA is described in the Supplementary Note. Supplementary Fig. 5 shows the displacement contour of the Si pellet array on the balloon stamp after picking up. The relative displacements of Si pellets caused by picking up are very small due to the much smaller size of the Si pellet array compared with that of the balloon stamp, resulting in minimal array distortion at the periphery of the array (Supplementary Fig. 6). The maximum principle strain contour of the Si pellet array on the balloon stamp after picking up is shown in Figure 1d and Supplementary Fig. 7a (top view). The strain in all the Si pellets is less than 0.01%, which is far smaller than the fracture strain of Si (~ 1%)[27,28]. The strain contours of the balloon and Clearflex outer layer after picking up the Si pellet array are shown in Supplementary Fig. 7b and c, respectively. After CAS printing on the hemispherical Ecoflex shell, the magnitude of the relative displacement contour of the Si pellet array is shown in Supplementary Fig. 8a. The corresponding strain distribution is shown in Fig. 1e and Supplementary Fig. 8b (top view) and Fig. S9 (perspective view).

The results show that the central region of the array has relatively lower strain than the peripheral area because the deformation in the balloon stamp increases from the initial contact region (central region of the array) to the outer areas. During conformal contact of the stamp, the central region of the array contacts on the top/center of the hemispherical shell and thus the deformation is restrained, while the periphery region of the array further deforms with the balloon stamp before contacting to the shell. The deformation and strain distribution in the latex balloon and Clearflex layer during transfer printing are shown in Supplementary Fig. 10. The Si pellet array originally in a planar configuration conforms to the curvy balloon stamp (after picking up) and the targeted hemispherical shell (after printing) surfaces, therefore, position distortion happens mainly in the peripheral area. Supplementary Fig. 11 compares the top views of the array prepared on the Si wafer (gray) and after CAS printing onto the curvy shell (green).

Hemispherical shaped photodetector array by CAS printing

A convex shaped photodetector array has implications in promising yet technically challenging and unusual imaging devices, e.g. wide angle of view imager. We demonstrated an array of Si photodetectors on a hemispherical shell by CAS printing. The Si photodetector was structured into two p-n junctions in back-to-back (n^+-p^--p^--n^+) configuration. The array (39 × 39, each Si photodetector size: 100 µm × 100 µm) was fabricated by selective doping to define the p-n junctions and then the same was done for the Si pellets. The processes are schematically shown in Supplementary Fig. 12 and also described in the Methods. Figures 2a and b show the optical images of the Si photodetector array on an Ecoflex hemispherical shell. The inset of Fig. 2a shows the photodetector array on the wafer before CAS printing. The performances of the photodetectors on hemispherical shell were examined as shown in Supplementary Fig. 13. The current versus voltage (*I-V*) characteristics of the photodetector before (on the rigid substrate) and after (on the hemispherical shell) transfer printing are shown in Fig. 2c. The photocurrent under illumination was 0.15 µA and the dark current was 449 pA at a 3 V bias. The calculated current ratio $\Delta I/I_0$ is 3.33×10^2 at a 3 V bias, which is defined by the ratio between photocurrent (current under illumination ($I_{illumination}$) – current in dark (I_{dark})) and dark current (I_{dark})[23,29,30]. The dynamic photocurrent responses of the device before and after CAS printing were measured at a constant bias of 3 V for 35 s while the light was respectively turned on/off. As shown in Fig. 2d and e, no significant performance difference was observed after CAS printing on a curvy surface compared with those on the wafer, which further verifies that the strain on the Si photodetector is negligible.

Curvy helix antenna

Compact sized (in mm to cm range) electrically small antennas in 3D curvy shapes are an important class of devices for many application[10,31,32]. However, efficiently manufacturing them in a simple yet precise manner has been a longstanding challenge[33]. We demonstrated a convex shaped, 4-armed helix antenna based on CAS printing. The 3D helix antenna fabrication involves pre-fabricating the antenna in a planar format and then CAS printing into a hemispherical convex shape. The fabrication began with laminating 5 µm-thick copper (Cu) foil on a Polydimethylsiloxane (PDMS) (Sylgard 184) coated glass substrate, patterning by conventional photolithography, and a wet etching process. The detailed fabrication process is illustrated in Supplementary Fig. 14 and in the Methods. Using CAS printing, the antenna was successfully printed onto an Ecoflex hemispherical shell shown in Fig. 2f. The inset of Fig. 2f shows an optical image of the pre-fabricated helix antenna on a glass substrate. Supplementary Fig. 15 shows the characterization setup, where one arm was soldered to the inner conductor of an SMA connector, and the other 3 arms were soldered to a circular copper ground plane with a radius of 9.2 cm. Figure 2g shows the measured reflection coefficient S11. The resonant frequency is 4.09 GHz and the half power bandwidth is 13.94%. The half power bandwidth is lower than -3 dB. The results clearly show a simple way of accomplishing a 3D helix antenna based on CAS printing.

Hemispherical solar cell

Solar cells in spherical or hemispherical shapes have unique advantages in terms of wide angle light harvesting compared with conventional planar devices[34-36]. We demonstrated a hemispherical shaped, thin Si based solar cell using CAS printing. The solar cell employs Si p-i-n junction devices connected in parallel and was pre-fabricated by selective doping, photolithography, RIE, anchor formation, and undercut etching on an SOI wafer. Then, the device array was transferred onto a thin polyimide film (~1.5 μm-thick) on a glass substrate by a PDMS stamp[22,37]. Thereafter, Au interconnects for the parallel connections were formed by e-beam evaporation and followed by PI encapsulation and patterning. The detailed device fabrication is described in the Methods and schematically illustrated in Supplementary Fig. 16. The patterned p-i-n Si solar cell array was released by BOE (6:1) and transferred to a temporary glass substrate as shown in Supplementary Fig. 17. The solar cell is designed in the fashion of Si device pixels with serpentine shaped interconnects, which are able to accommodate the large deformation during the CAS process without cracking the brittle Si devices. Finally, the solar cell array was printed onto a hemispherical PDMS shell through CAS printing as shown in Supplementary Fig. 18. Figure 3a provides a photograph of the hemispherical solar cell array and Fig. 3b shows an optical microscopic image of the interconnected solar cell pixels on the hemispherical shell. FEA was performed to evaluate the strain on the device. Fig. 3c presents the optical image of the Si p-i-n solar cell array (left) and the corresponding FEA simulated strain distribution (right). The interconnection experienced a maximum principal strain of ~1.48 % due to the deformation of the device array during the CAS printing process. However, the maximum principal strain for Si is ~0.18 % (Fig. 3d). In addition, the intrinsic Si region experienced negligible strain.

The hemispherical solar cell was tested under 100 mW/cm^2 (1 sun) in ambient conditions.

The current density versus voltage (*J*-*V*) characteristic of a single p-i-n pixel is shown in Fig. 3e. The short circuit current density (J_{sc}), open circuit voltage (V_{oc}), fill factor (*FF*), and photocurrent-conversion efficiency are 14.46 mA/cm^2, 0.352 V, 50.39%, and 2.56%, respectively. The *I*-*V* and output power-voltage curves of the single solar cell are shown in Supplementary Fig. 19. Figure 3f shows the output power-voltage curve of the interconnected solar cell array in a planar configuration before printing onto the hemispherical shell. The short circuit current (I_{sc}), V_{oc}, *FF*, and maximum power are 0.66 mA, 0.303 V, 34.11%, and 68.3 μW, respectively. After CAS printing, the yielded hemispherical solar cell was characterized under different incident angles of light (Supplementary Fig. 20). The *I*-*V* characteristics and output power-voltage curve of the hemispherical solar cell depending on the incident angle of light are shown in Supplementary Fig. 21 and Fig. 3f, respectively. The maximum output powers are 39.0 μW, 28.2 μW, 20.8 μW, and 10.7 μW at 90°, 60°, 30°, and 0° incident angles of light, respectively. It is noted that the maximum power of the hemispherical solar cell at 90° of incident light angle is lower than that of a device in planar configuration due to the device footprint and thus the exposed area difference.

Multifunctional contact lens

Contact lenses with enabled noninvasive health monitoring or imaging functions are promising smart wearable devices. A prototype of a smart contact lens (Figure 4a) with three different devices including a (i) lactate sensor, (ii) temperature sensor, and (iii) imager was achieved using CAS printing onto the molded PDMS lens model. Specifically, unusual high L-lactate concentration in tears provides a possible indication of ischemia, sepsis, liver disease, and/or even cancer[6,38]. Significantly higher L-lactate concentration in tear fluid (1 – 5 mM) than that in blood (0.36 – 0.75 mM)[6] correspondingly makes the sensor development less challenging, therefore it is advantageous to implement lactate sensing based on non-invasive contact lenses. The ocular surface temperature (OST) is one of the crucial parameters for diagnosing eye health conditions since it relates to blood-flow velocity in the ophthalmic artery[39]. Image capturing from a worn contact lens is a unique feature as it can either supplement or enable visual capabilities for the wearer. All sensors and imager were pre-fabricated based on microfabrication, then printed onto a contact lens using CAS printing, as aforementioned for the other devices. The detailed fabrication process is described in Methods and schematically illustrated in Supplementary Fig. 22-24. The successfully fabricated smart contact lens is shown in Fig. 4b.

The lactate sensor based on the amperometric mechanism was structured with three electrodes, including a working electrode (WE), a counter electrode (CE), and a reference electrode (RE). The WE and CE were designed into serpentine shapes to enable mechanical stretchability. A thin layer of lactate oxidase (LOx) as the enzyme on the electrodes is shown in Fig. 4c. The inset of Figure 4c schematically shows the sensing mechanism. The details are described in the Supplementary Note. The amperometric measurements were performed with a constant potential of 400 mV at the RE by varying the concentration of the L-lactate solution. Continuous sensing of tear L-lactate concentration in the physiological range (1 - 5 mM)[6,38] was successfully achieved (Fig. 4d). It is noted that at relatively low concentrations (0.05 - 1 mM), a linear response between the current and concentration was observed (Supplementary Fig. 25). At higher concentrations (1 - 50 mM), a nonlinear relationship was observed (Supplementary Fig. 26). The calculated sensitivity and limit of detection (LOD) of the sensor are 9.39 μA/ cm^2·mM and 4.57 μM, respectively. The measurements were further compared with the Michaelis-Menten Kinetic model[38,40]. Specifically, the Michaelis-Menten constant (K_M) and I_{MAX} were extracted from Supplementary Fig. 26a using the Lineweaver-Burk equation and the values are 1.23 mM and

113.62 nA, respectively[40,41]. The detailed calculations are described in the Supplementary Note. The fitting curve of the Michaelis-Menten Kinetic model is in good agreement with the measurements, as shown in Fig. 4e and Supplementary Fig. 26b. The results suggest that the contact lens with a lactate sensor is feasible for continuous monitoring of the L-lactate level in tear fluid.

The temperature sensor for OST monitoring was based on a Si p-i-n diode. The device is interconnected with serpentine electrodes, as shown in Fig. 4f. A light blocking layer of metal was used to eliminate any photo response. Figure 4g shows the I-V curves of the diode temperature sensor under different temperatures (26 ºC, 36 ºC, and 46 ºC). Clear temperature dependency on the forward biased current was shown[42,43]. The calibration curve was obtained by extracting voltage at 1 μA from the I-V curves under different temperatures as shown in Supplementary Fig. 27. Figure 4i shows continuous temperature sensing based on the diode sensor. The result matches well with that of a thermocouple (Fluke 80PK-1 Bead Probe).

The imager was designed with 8 × 8 arrayed photo detecting pixels (Fig. 4j). The individual pixel consists of a Si p-i-n photodiode and n-i-p multiplexing diode configured in a back-to-back fashion. The multiplexing diode has a metal light blocking layer to eliminate its light response (Inset of Fig. 4j). Figure 4k shows the I-V curves of an individual pixel under illumination and in the dark with a photocurrent of 1.02 μA and a dark current of 3.95 nA. Supplementary Fig. 28 shows the circuit diagram of the imager with the detector array, where shunt resistors (5 MΩ) were used for voltage measurement purposes. It is noted that –1 V was applied to each column during readout. The dynamic output voltage upon repeatedly turning the light on/off for a single pixel is shown in the Supplementary Fig. 29. Multiplexing enabled voltage mapping from patterned light illumination through a photomask was obtained based on a data acquisition system (DAQ, National Instruments)[44]. Figure 4l illustrates the voltage mapping based on illumination through a “cross” shaped photomask (inset).

CAS printing on arbitrary curvy surfaces

Although several different hemispherical or similarly shaped devices were demonstrated, we further validated the versatility and fidelity of CAS printing devices onto arbitrary 3D surfaces. Serpentine shaped meshes (Supplementary Fig. 30; overall size 11.2 mm × 11.2 mm) with a metal layer sandwiched between two polyimide layers were used. The processes of mesh fabrication are described in the Methods and schematically shown in Supplementary Fig. 31. Various 3D curvy surfaces including concave, wavy, convex edge, concave edge, pyramid, and uneven surface were prepared with a thin adhesive layer of Ecoflex. The meshes were successfully printed onto these curvy substrates as shown in Fig. 5a-f. The versatility of CAS printing onto arbitrary curvy or uneven substrates is owed to the conformal contact between the stamp and target surfaces. FEA was also carried out to simulate the deformation and strain within the stamp and mesh. The relative displacement contour of the mesh on the stamp after picking up is shown in Supplementary Fig. 32. In addition, the strain distributions of the balloon, coating layer, and mesh on the balloon stamp are shown in Supplementary Fig. 33. During CAS printing onto concave and screwdriver handle wavy surfaces, the strain distribution of the balloon and coating layer are illustrated in Supplementary Fig. 34 (concave) and Supplementary Fig. 35 (wavy), respectively.

The bottom frames of Figs. 5a and b show the strain distribution in the metal layer after printed onto the concave and screwdriver handle wavy surfaces, respectively. The maximum strain in Fig. 5a is ~1.33 % near the corners, which is because the serpentine mesh is mainly subject to bending with relatively large stretching in the four corners (Supplementary Fig. 36). Compared to the concave substrate, the screwdriver handle has sharper edges, causing more severe deformation in the metal mesh during the CAS printing process as shown in Fig. 5b and Supplementary Figs. 35 and 37. The maximum strain in the metal mesh is 3.28%, appearing on the edges. The mesh near the edges of the handle is subjected to a combination of bending and stretching. These results evidentially suggest that CAS printing induces tolerant strain into devices and can be employed as a generalized platform for devices with various curvy shapes.

Discussion

In this work, we developed and systematically investigated the CAS printing technology for reliably manufacturing 3D curvy electronics in a simple, reliable and effective way. CAS printing has been validated to be effective for manufacturing curvy devices with both isolated pixels, such as thin Si pellets and photodetector arrays, and interconnected functional devices including antennas, hemispherical solar cells, and smart contact lenses. Taking advantage of traditional electronics fabrication, 3D curvy electronics from CAS offers high performance, outperforming the existing 3D printing technologies with liquid or semiliquid based electronic materials[8]. The excellent deformability of the balloon stamp is a key feature that renders the versatility of CAS printing for manufacturing onto arbitrary 3D surfaces. CAS printing clears the roadblocks for 3D curvy electronics and holds great promise in enabling unprecedented devices and systems in many fields, such as optoelectronics, telecommunication, medical, etc.

Methods

Conformal balloon stamp preparation.

The balloon stamp was prepared by inflating a latex balloon. Liquid Clearflex precursor (Smooth-ON, Clear Flex^{TM} 50) was coated on the inflated balloon and pre-cured at room temperature for 16 hrs and then fully cured at 60 ^{o}C for 5 hrs.

Hemispherical shell preparation.

The hemispherical shell was prepared using a custom-made mold. Liquid silicone, such as Ecoflex (Smooth-On Ecoflex 00-30) or PDMS (Sylgard 184, ratio of monomer to crosslinker is 10:1), was poured into a concave mold. Then a convex mold was pressed against the concave mold with a 1 mm thick spacer. The mold was heated at 90 ^{o}C to solidify for 20 min or 60 min for Ecoflex or PDMS, respectively. Finally, the shell was retrieved by separating the molds.

Si pellet array fabrication.

The Si pellet array was prepared from an SOI wafer with 1.25 μm-thick single crystalline Si on top. The fabrication of the 39 × 39 array of Si square pellets (100 μm × 100 μm) were started by photolithography to define the geometries. The photolithography process involved spin-coating of photoresist (AZ 5214) on the SOI wafer at 2000 rpm for 30 s and baking on a hotplate at 110 ^{o}C for 90 s, followed by UV exposure (λ = 365 μm) with a dose of 200 mJ cm^{-2}, and developing through MIF917 for 1 min. Thereafter, the Si pellet array was patterned by reactive ion etching (RIE) by sulfur hexafluoride (SF_6) with a gas flow of 100 sccm for 1 min. The photoresist anchors for Si pellets were formed by photolithography after etching the exposed SiO_2 by BOE (6:1) in order to prevent the floating away of the pellet after fully undercut etching of the SiO_2. The Si pellet array was immersed in concentrated hydrofluoric acid (HF, 49%) for 90 min to fully remove the buried SiO_2.

Si photodetector fabrication.

The Si based photodetector array fabrication began with cleaning the SOI wafer with 1.25 μm thick top Si (p-type, resistivity: 11.5 Ω cm) for selective doping. A 300 nm-thick SiO_2 based doping mask was formed on the SOI wafer using spin-on-glass (700B, Filmtronics), followed by annealing at 700 °C for 4 min in N_2 atmosphere. The doping windows were opened by photolithography and wet etch in BOE (6:1) for 1 min. The phosphorous based spin-on-dopant (P510, Filmtronics) was coated and annealed at 950 °C to form two back to back n^+-p^--p^--n^+ diodes. The photodetector array was patterned and released from the Si wafer following the same procedures for the Si pellet array.

Copper antenna fabrication.

The antenna was accomplished by fabricating on a temporary substrate of PDMS. PDMS precursor solution (Sylgard 184, ratio of monomer to crosslinker is 10:1) was spin coated on a glass substrate followed by half-curing at 100 °C for 30 s. A 5 μm-thick Cu foil was carefully laminated on top of the PDMS/grass substrate followed by full curing to ensure stable bonding. The antenna was patterned through photolithography and wet etching by Cu etchant. The antenna was picked up using scotch tape and released onto a glass substrate in acetone solution[21].

Silicon solar cell array.

The fabrication of Si solar cell follows similar steps as that for the photodetectors, except both n- and p-type doping are performed. Spin-on-glass (700B, Filmtronics) was used as doping mask and p-type doping was first processed using boron based spin-on-dopant (B155, Filmtronics) annealed at 950 ^{o}C. The dopant residue and SiO_2 doping mask was removed by concentrated HF. The n-doping mask was formed by Spin-on-glass and the n-doping was based on spin-on-dopant (P510, Filmtronics). The spacing between p-doping and n-doping was 30 μm, thus intrinsic region for light harvesting is defined as 4.5×10^{-5} cm^2. The top Si device was patterned into 150 μm × 150 μm square arrays by RIE using SF_6 gas (100 sccm for 1 min). The released p-i-n solar cell array was picked up by a PDMS stamp (~8 mm thickness) and transfer printed on top of half-cured PI layer on a glass substrate. The PI was then fully cured at 250 ^{o}C for 1 hr. Interconnects of Cr (5 nm) and Au (200 nm) were deposited on the transferred devices array using e-beam evaporator and patterned by photolithography. Then, devices are encapsulated by another PI using spin-casting, photolithography and RIE etching in O_2 plasma. Finally, the solar cell array was released from the glass substrate by immersion in BOE solution.

Multifunctional contact lens fabrication

The contact lens electronics with multiple functions (lactate sensing, temperature sensing, and imaging sensing) was fabricated through similar process as abovementioned photodetector array and p-i-n solar cells. The three sensors were fabricated simultaneously. The fabrication process began with selective doping Si on a SOI wafer and transfer printing onto a half-cured PI substrate as abovementioned. After transfer printing, the PI was fully cured at 250 ^{o}C for 1 hr. Then a PI interlayer was coated and formed via hole using RIE (O_2, 40 sccm, 150 mTorr, 250 W, 10 min). The first interconnecting metal (Cr/Au, 5/200 nm) was formed using e-beam evaporation, photolithography, and wet etching. Then, another PI layer was formed and the second via hole was formed, followed by second metallization (Cr/Au, 5/200 nm) for another interconnection and light blocking layer for blocking diode and temperature sensor. Thereafter, an encapsulating PI layer was coated on top of the devices and cured. The devices were patterned using O_2 plasma through a SiO_2 mask that was formed by e-beam evaporation and photolithography. The thin device was then separated from the glass substrate using buffer oxide etchant (BOE, 6:1). The separated device was retrieved by a balloon stamp and printed onto UVO treated contact lens model, followed by thermal treatment at 90 °C to form irreversible bonding. To form LOx on the lactate sensor electrodes, the LOx was immobilized by covalent cross-linking of the enzyme and bovine serum albumin (BSA) by glutaraldehyde (GTA)[38]. 2.55 mg BSA ($\geq$ 98%, lyophilized powder, Sigma Aldrich) was dissolved in 79.73 µl phosphate buffer solution (PBS). Then, 1.02 µl GTA (25% in H_2O, Grade I, Sigma Aldrich) and 1.7 mg lactate oxidase from Aerococcus viridans (50UN, lyophilized powder, Sigma Aldrich) were added in the solution. The solution was dropped onto the electrodes, then dried for 1 hr at room temperature.

Serpentine mesh fabrication.

The mesh started with coating PI precursor solution and cured at 250 °C for 1 hr. 200 nm of Cu layer was deposited on the PI by e-beam evaporator. The Au layer was then patterned by photolithography and wet etching. The PI with metal on top was finally patterned and released from the glass substrate.

Si photodetector characterization.

Electrical characteristics of Si-photodetectors were measured by Keithley 2400 source meter with Imagelite model 20 illuminator (Stocher & Yale) light source at room temperature under ambient condition.

Copper antenna characterization.

The reflection coefficient of the helix antenna was measured by National Instrument PXIe-5630 vector network analyzer in free space. The antenna was placed on a copper ground and fed by an SMA probe.

Hemispherical solar cell characterization.

The *J*-*V* curves and output power of the p-i-n Si solar cells were characterized under 1 sun light condition using a Keithley 2400 source meter and a solar simulator (ORIEL Instruments, Sol3A). A standard silicon solar cell (ORIEL, 91150V) was used to calibrate the power of the 1 sun simulated light (100 mW/cm^2). Hemispherical solar cell performances with different light incident angle were measured by tilting the device.

Acknowledgement

C.Y. would like to thank the funding support by National Science Foundation (ECCS-1509763 and CMMI-1554499), startup and the Bill D. Cook faculty scholarship from the Department of Mechanical Engineering at University of Houston.

Author Contributions

K.S., S.C. and C.Y. conceived and designed the experiment. K.S., S.C., Z.R., J.L., Y.L., and S.J. performed the experiment. Z.L., and J.X. performed numerical analysis. K.S., J.C., and C.Y. analyzed experimental data. K.S., Z.L., J.X., F.E., and C.Y. wrote the paper.

Competing financial interests

The authors declare no competing financial interests.

References

1 Dinyari, R., Rim, S.-B., Huang, K., Catrysse, P. B. & Peumans, P. Curving monolithic silicon for nonplanar focal plane array applications. *Appl. Phys. Lett.* **92**, 091114 (2008).

2 Hung, P. J., Jeong, K., Liu, G. L. & Lee, L. P. Microfabricated suspensions for electrical connections on the tunable elastomer membrane. *Appl. Phys. Lett.* **85**, 6051-6053 (2004).

3 Song, Y. M. *et al.* Digital cameras with designs inspired by the arthropod eye. *Nature* **497**, 95-99 (2013).

4 Jeong, K.-H., Kim, J. & Lee, L. P. Biologically inspired artificial compound eyes. *Science* **312**, 557-561 (2006).

5 Kim, J. *et al.* Wearable smart sensor systems integrated on soft contact lenses for wireless ocular diagnostics. *Nat. Commun.* **8**, 14997 (2017).

6 Farandos, N. M., Yetisen, A. K., Monteiro, M. J., Lowe, C. R. & Yun, S. H. Contact lens sensors in ocular diagnostics. *Adv. Healthc. Mater.* **4**, 792-810 (2015).

7 Vásquez Quintero, A., Verplancke, R., De Smet, H. & Vanfleteren, J. Stretchable Electronic Platform for Soft and Smart Contact Lens Applications. *Adv. Mater. Technol.* **2**, 1700073 (2017).

8 Adams, J. J. *et al.* Conformal Printing of Electrically Small Antennas on Three-Dimensional Surfaces. *Adv. Mater.* **23**, 1335-1340 (2011).

9 Kim, O. S. Low-Q electrically small spherical magnetic dipole antennas. *IEEE Trans. Antennas Propag.* **58**, 2210-2217 (2010).

10 Abadia, J., Merli, F., Zurcher, J.-F., Mosig, J. R. & Skrivervik, A. K. 3D-spiral small antenna design and realization for biomedical telemetry in the MICS band. *Radioengineering* **18**, 359-367 (2009).

11 Boncheva, M. *et al.* Magnetic self-assembly of three-dimensional surfaces from planar sheets. *Proc. Natl. Acad. Sci. U.S.A* **102**, 3924-3929 (2005).

12 Guo, X. *et al.* Two-and three-dimensional folding of thin film single-crystalline silicon for photovoltaic power applications. *Proc. Natl. Acad. Sci. U.S.A* **106**, 20149-20154 (2009).

13 Xu, W. *et al.* Ultrathin thermoresponsive self-folding 3D graphene. *Sci. Adv.* **3**, e1701084 (2017).

14 Liu, Y., Shaw, B., Dickey, M. D. & Genzer, J. Sequential self-folding of polymer sheets. *Sci. Adv.* **3**, e1602417 (2017).

15 Mei, J., Lovell, M. R. & Mickle, M. H. Formulation and processing of novel conductive solution inks in continuous inkjet printing of 3-D electric circuits. *IEEE Trans. Electron. Packag. Manuf.* **28**, 265-273 (2005).

16 Seong, B. *et al.* Metal-mesh based transparent electrode on a 3-D curved surface by electrohydrodynamic jet printing. *J. Micromech. Microeng.* **24**, 097002 (2014).

17 An, B. W. *et al.* Direct printing of reduced graphene oxide on planar or highly curved surfaces with high resolutions using electrohydrodynamics. *Small* **11**, 2263-2268 (2015).

18 Ko, H. C. *et al.* Curvilinear electronics formed using silicon membrane circuits and elastomeric transfer elements. *Small* **5**, 2703-2709 (2009).

19 Ko, H. C. *et al.* A hemispherical electronic eye camera based on compressible silicon optoelectronics. *Nature* **454**, 748-753 (2008).

20 Huang, C. C. *et al.* Large field of view wide spectrum artificial reflecting superposition compound eyes. *Small* **10**, 3050-3057 (2014).

21 Sim, K. *et al.* High Fidelity Tape Transfer Printing Based On Chemically Induced Adhesive Strength Modulation. *Sci. Rep.* **5**, 16133 (2015).

22 Sim, K., Li, Y., Song, J. & Yu, C. Biaxially Stretchable Ultrathin Si Enabled by Serpentine Structures on Prestrained Elastomers. *Adv. Mater. Technol.* **4**, 1800489 (2019).

23 Sim, K., Rao, Z., Li, Y., Yang, D. & Yu, C. Curvy surface conformal ultra-thin transfer printed Si optoelectronic penetrating microprobe arrays. *npj Flex. Electron.* **2**, 2 (2018).

24 Gao, Y. *et al.* Crack-Insensitive Wearable Electronics Enabled Through High-Strength Kevlar Fabrics. *IEEE Trans. Compon. Packag. Manuf. Technol.* **5**, 1230-1236 (2015).

25 Xu, S. *et al.* Assembly of micro/nanomaterials into complex, three-dimensional architectures by compressive buckling. *Science* **347**, 154-159 (2015).

26 Wang, X. *et al.* Freestanding 3D Mesostructures, Functional Devices, and Shape-Programmable Systems Based on Mechanically Induced Assembly with Shape Memory Polymers. *Adv. Mater.* **31**, 1805615 (2019).

27 Zhang, Y. *et al.* A mechanically driven form of Kirigami as a route to 3D mesostructures in micro/nanomembranes. *Proc. Natl. Acad. Sci. U.S.A* **112**, 11757-11764 (2015).

28 Humood, M. *et al.* Fabrication and Deformation of 3D Multilayered Kirigami Microstructures. *Small* **14**, 1703852 (2018).

29 Qian, C. *et al.* High-Performance Organic Heterojunction Phototransistors Based on Highly Ordered Copper Phthalocyanine/para-Sexiphenyl Thin Films. *Adv. Funct. Mater.* **27**, 1604933 (2017).

30 Noh, Y.-Y., Kim, D.-Y. & Yase, K. Highly sensitive thin-film organic phototransistors: Effect of wavelength of light source on device performance. *J. Appl. Phys.* **98**, 074505 (2005).

31 Adams, J., Slimmer, S. C., Lewis, J. & Bernhard, J. 3D-printed spherical dipole antenna integrated on small RF node. *Electron. Lett* **51**, 661-662 (2015).

32 Toriz-Garcia, J. *et al.* Fabrication of a 3D electrically small antenna using holographic photolithography. *J. Micromech. Microeng.* **23**, 055010 (2013).

33 Liu, F. *et al.* High Performance, Tunable Electrically Small Antennas through Mechanically Guided 3D Assembly. *Small* **15**, 1804055 (2019).

34 Lamoureux, A., Lee, K., Shlian, M., Forrest, S. R. & Shtein, M. Dynamic kirigami structures for integrated solar tracking. *Nat. Commun.* **6**, 8092 (2015).

35 Maruyama, T. & Minami, H. Light trapping in spherical silicon solar cell module. *Sol. Energy Mater. Sol. Cells* **79**, 113-124 (2003).

36 Minemoto, T., Murozono, M., Yamaguchi, Y., Takakura, H. & Hamakawa, Y. Design strategy and development of spherical silicon solar cell with semi-concentration reflector system. *Sol. Energy Mater. Sol. Cells* **90**, 3009-3013 (2006).

37 Meitl, M. A. *et al.* Transfer printing by kinetic control of adhesion to an elastomeric stamp. *Nat. Mater.* **5**, 33 (2005).

38 Thomas, N., Lähdesmäki, I. & Parviz, B. A. A contact lens with an integrated lactate sensor. *Sens. Actuators, B* **162**, 128-134 (2012).

39 Gugleta, K., Orgül, S. & Flammer, J. Is corneal temperature correlated with blood-flow velocity in the ophthalmic artery? *Curr. Eye Res.* **19**, 496-501 (1999).

40 Kausaite-Minkstimiene, A., Mazeiko, V., Ramanaviciene, A. & Ramanavicius, A. Enzymatically synthesized polyaniline layer for extension of linear detection region of amperometric glucose biosensor. *Biosens. Bioelectron.* **26**, 790-797 (2010).

41 Yu, J., Liu, S. & Ju, H. Glucose sensor for flow injection analysis of serum glucose based on immobilization of glucose oxidase in titania sol–gel membrane. *Biosens. Bioelectron.* **19**, 401-409 (2003).

42 Kim, J. *et al.* Stretchable silicon nanoribbon electronics for skin prosthesis. *Nat. Commun.* **5**, 5747 (2014).

43 Webb, R. C. *et al.* Ultrathin conformal devices for precise and continuous thermal characterization of human skin. *Nat. Mater.* **12**, 938 (2013).

44 Yu, C. *et al.* Adaptive optoelectronic camouflage systems with designs inspired by cephalopod skins. *Proc. Natl. Acad. Sci. U.S.A* **111**, 12998-13003 (2014).

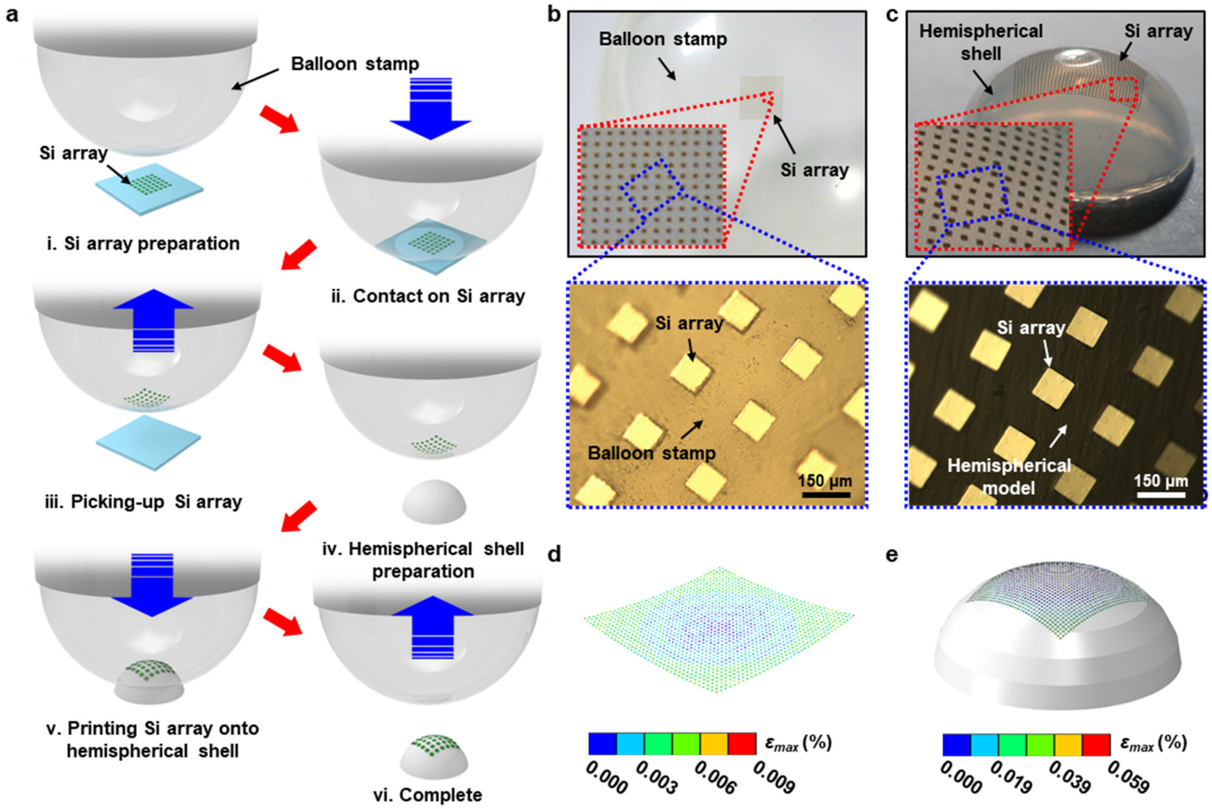

Fig 1. CAS printing. a, Schematic illustration of CAS printing. **b,** The retrieved Si pellet array on a balloon stamp. **c,** CAS printed Si pellet array on a hemispherical shell. **d,** Maximum principal strain contour in the Si pellet array on a balloon stamp after picking up from an SOI wafer. **e,** Maximum principal strain contour in the Si pellet array on a hemispherical Ecoflex shell after CAS printing.

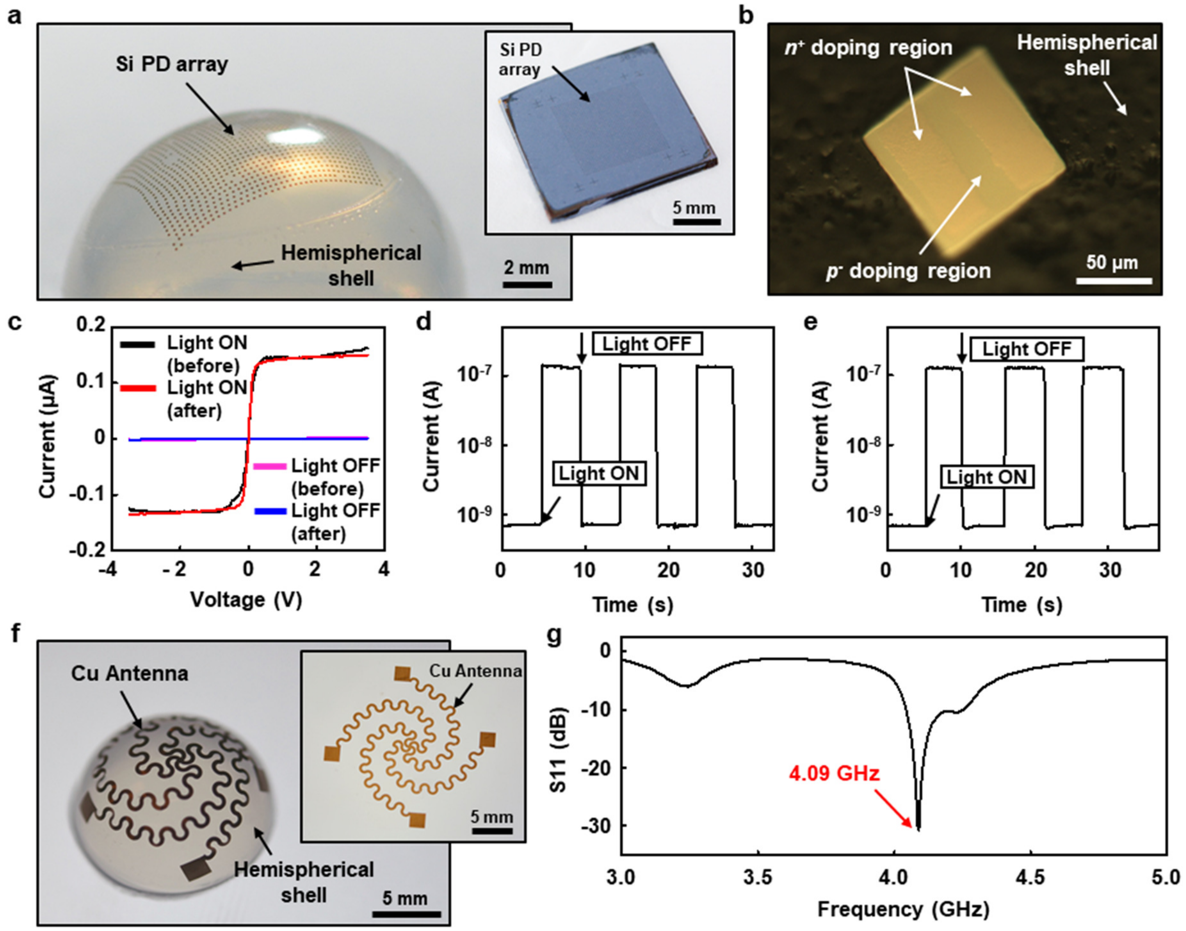

Fig. 2. Devices on a hemispherical shell by CAS printing. a, A photo image of the Si photodetector array on a hemispherical shell after CAS printing. Inset is the photodetector array on an SOI substrate. **b,** An optical microscopic image of one single Si photodetector on a hemispherical shell. **c,** *I*-*V* curves of the photodetector under illumination and in the dark before and after CAS printing. **d-e** ,Dynamic photoelectrical responses of the photodetector before (**d**) and after (**e**) CAS printing. **f,** An optical image of a 3D Cu helix antenna fabricated by CAS printing. Inset is an optical image of a Cu helix antenna on a planar substrate. **g,** The measured reflection coefficient S11 of the 3D helix antenna.

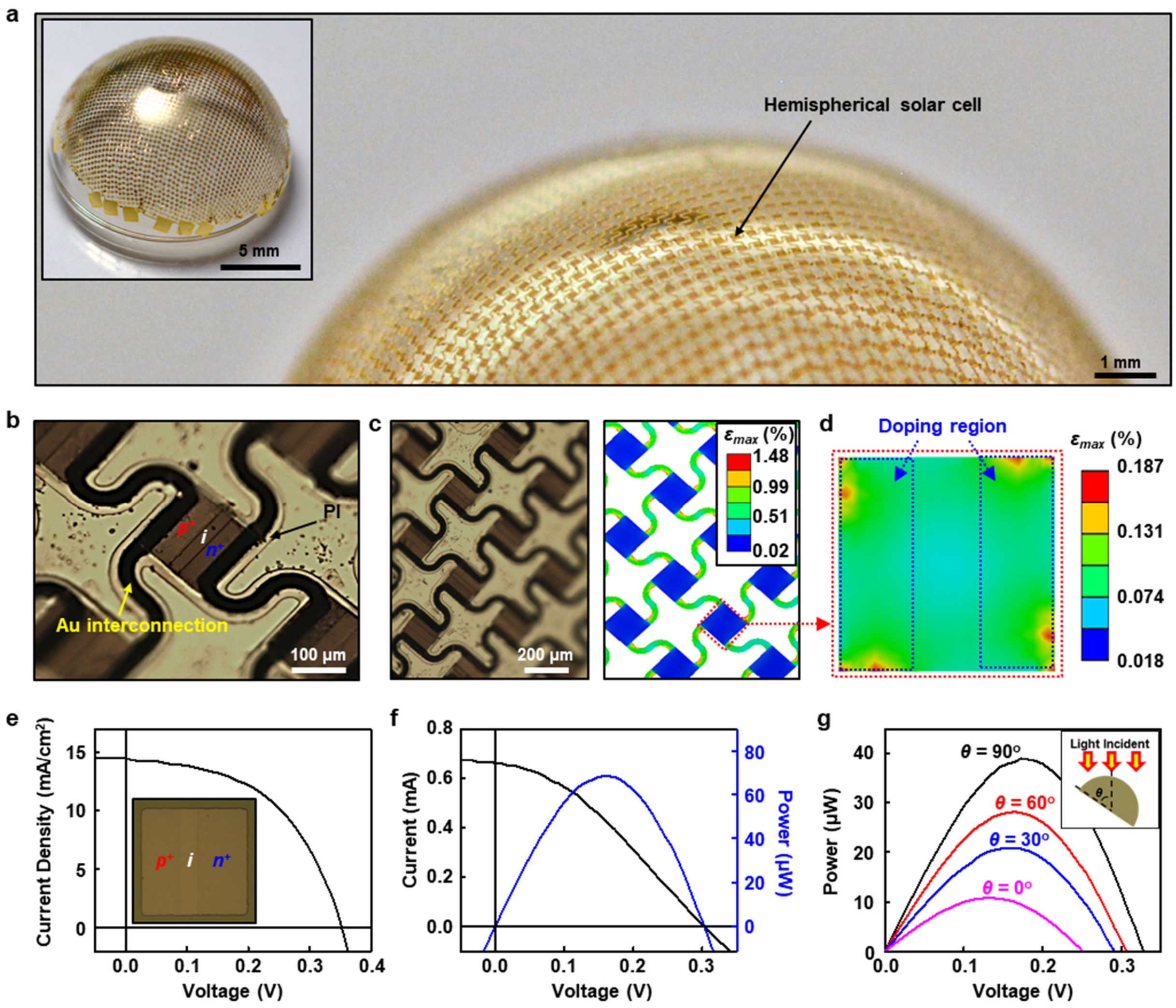

Fig. 3. Hemispherical solar cell. a, An optical image of the Si based p-i-n solar cell array on a hemispherical PDMS substrate after CAS printing. Inset is the overall view of the p-i-n solar cell array on a hemispherical PDMS substrate. **b,** An optical microscopic image of a single Si based p-i-n solar cell. **c,** An optical microscopic image of a Si based p-i-n solar cell array on hemispherical substrate (left) and the corresponding FEA result (right). **d,** The FEA result of the maximum principle strain in the interconnected Si based p-i-n solar cells. **e,** The *J*-*V* curve of a single p-i-n Si solar cell. Inset is an optical microscopic image of single solar cell before interconnection. **f,** The *I*-*V* curve and output power-voltage curve of the interconnected solar cell array on a planar substrate. **g,** Output power-voltage curve of the interconnected solar cell array on a hemispherical

substrate after CAS printing depending on incident angles of light. Inset is a schematic drawing of incident angle of light definition.

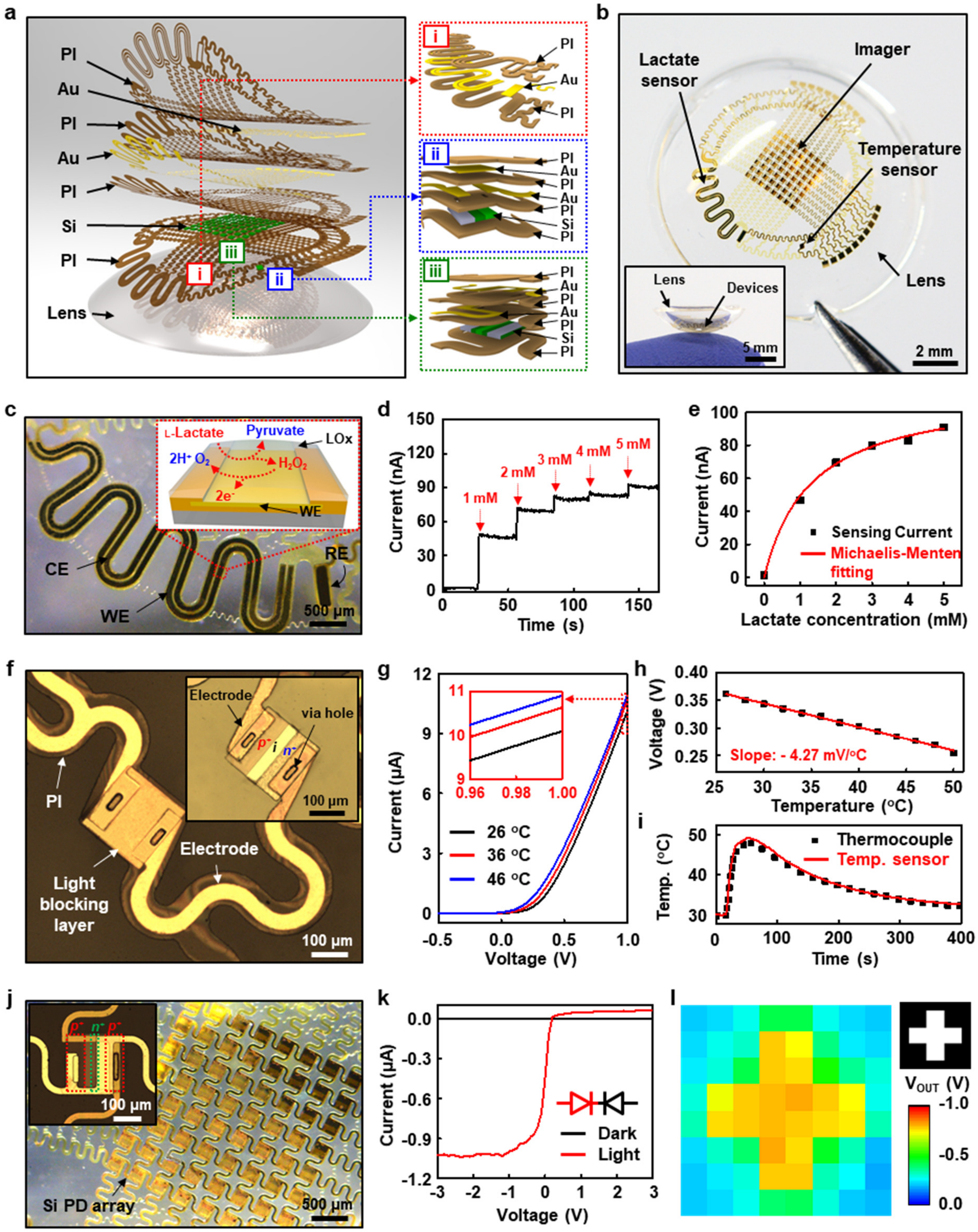

Fig. 4. Multiple functional smart contact lens electronics. a, Schematic illustration of the contact lens electronics. **b,** Optical image of the contact lens electronics. Inset is a side view of the

electronics. **c,** Optical microscopic image of the lactate sensor. Inset is a schematic illustration of the sensing mechanism. **d,** Continuous sensing properties depending on the L-lactate concentration. **e,** Calibration curve of the lactate sensor in the physiological range (1 - 5 mM) with a fitting curve from the Michaelis-Menten model. **f,** Optical microscopic image of the Si temperature sensor. Inset is the device before formation of the light blocking layer. **g,** I-V characteristics of the temperature sensor at different representative temperatures. **h,** Calibration curve of Si temperature sensor. **i,** Plots of temperature sensing by using a commercially available thermocouple and Si based temperature sensor. **j,** Optical microscopic image of the imaging sensor array on the contact lens. Inset is an optical microscopic image of a single pixel. **k,** Representative *I-V* curve of a single pixel under illumination (light, red) and in the dark (black). **l,** Output voltage mapping result of the imaging sensor array under the patterned illumination through a photomask. Inset is the shape of photomask.

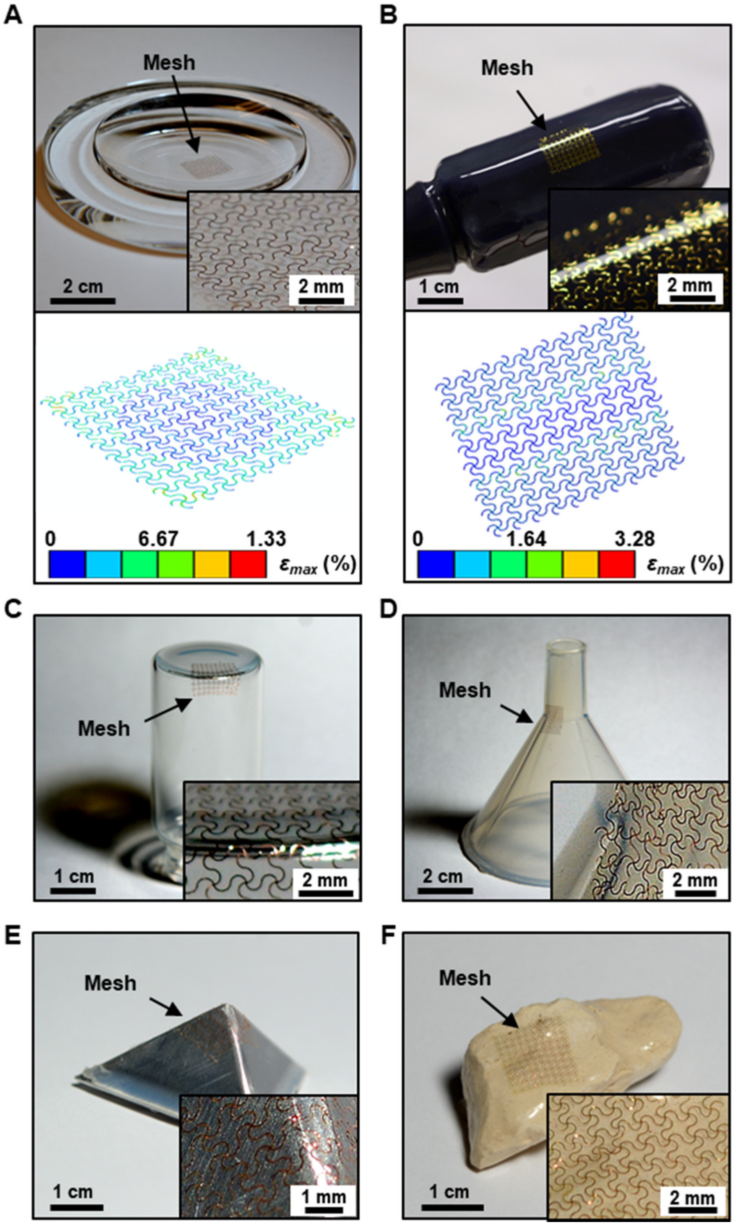

Fig. 5. CAS printing onto various 3D curvilinear substrates. **a-f,** Optical image of the serpentine metal mesh on concave (**a, top**), wavy (**b, top**), convex edge (**c**), concave edge (**d**), pyramid (**e**), and uneven surfaces (**f**) by CAS printing. FEA results of the serpentine metal mesh on concave (**a, bottom**), and wavy (**b, bottom**) surfaces by CAS printing.